Journal of Materials Chemistry A

RSC Publishing

PAPER

View Article Online
View Journal | View Issue

Metallocene/carbon hybrids prepared by a solution process for supercapacitor applications†

Cite this: *J. Mater. Chem. A*, 2013, **1**, 13120

Xianwen Mao, Fritz Simeon, Demetra S. Achilleos, Gregory C. Rutledge* and T. Alan Hatton*

Received 25th August 2013
Accepted 10th September 2013

DOI: 10.1039/c3ta13361c

www.rsc.org/MaterialsA

Efficient and scalable solution-based processes are not generally available to integrate well-studied pseudocapacitive materials (*i.e.*, metal oxides and conducting polymers) with other components such as porous carbon, mainly because these classes of pseudocapacitive systems have poor solubilities in solvents and exhibit no specific interactions with the other component. Here we report, for the first time, the integration of a metallocene polymer, polyvinylferrocene (PVF), with carbon nanotubes (CNTs) *via* a simple solution process for supercapacitor applications. The solution processability of the PVF/CNT hybrid is due to the high solubilities of PVF in organic solvents and the unique ability of the metallocene/carbon system to form stable dispersions through the π–π stacking interactions between the two components. The nanostructure and electrochemical properties of the hybrid can be manipulated systematically by adjusting the composition of the dispersion. The hybrid with the optimized composition exhibits unusually high capacitance (1452 F g^{-1}) and energy density (79.5 W h kg^{-1}) obtained in a standard two-electrode configuration, outperforming previously reported pseudocapacitive materials.

Introduction

Supercapacitors have attracted widespread attention as promising energy storage devices due to their high capacitance, long cycle life, fast response time, and exceptional reversibility and reliability.[1,2] These advantages allow supercapacitors to meet the challenge of delivering high currents in heavy-duty systems such as hybrid electric vehicles and large industrial equipment.[3] The large specific capacitance of supercapacitors results from two charge-storage mechanisms that occur at the electrode/electrolyte interface: double-layer capacitance, which is a non-Faradic process, and redox-based pseudocapacitance, which is a Faradic process. These two mechanisms can work separately or together. Carbon-based materials are well-known examples of double-layer capacitive materials,[1,2,4] while conducting polymers and metal oxides have been studied extensively as pseudocapacitive materials.[1,2,5] Recently, heterogeneous nanostructured materials have emerged as promising systems for electrochemical energy storage, due to the combined benefits of reduced inherent structure size of the bulk materials (*e.g.*, enhanced specific surface area and reduced ion diffusion length) and synergy of the properties of the individual components (*e.g.*, improved electron transport efficiency and mechanical stability).[6,7] Nanostructured hybrid supercapacitors with enhanced electrochemical properties have been created by controlled assembly of different capacitive materials, such as conducting polymer/carbon,[8–14] conducting polymer/metal oxide,[15] metal oxide/carbon,[16–18] metal oxide/metal oxide,[19] and metal oxide/metal.[20–22] When constructing these heterogeneous systems, the key to achieving optimal performance is the ability to manipulate their compositions and nanoscale architectures, and to assemble the individual components in a way that does not impair their respective advantageous features (*e.g.*, preservation of intrinsically high conductivity of the conducting component).[8–22]

Solution processes are low-cost, high-throughput, and readily scalable, and thus have been exploited to deposit various nanomaterials on appropriate substrates for large-scale applications, including solar cells,[23,24] thin-film transistors,[25–27] lithium-ion batteries,[28,29] and single-component supercapacitor devices.[29,30] However, it is very difficult to employ solution processes to construct heterogeneous nanomaterials based on well-studied pseudocapacitive materials (*i.e.*, metal oxides and conducting polymers), especially those with controlled morphology and electrocapacitive properties.[5–7] This is due to the poor solubilities of metal oxides and conducting polymers in most solvents, and lack of strong interactions between these pseudo-capacitive materials and other components (*e.g.*, carbon nanomaterials).[31,32] Thus, in general, different capacitive materials cannot form stable complexes in solvents, and it is difficult to generate well-dispersed, high-quality heterogeneous "inks" for solution processing. The common techniques for

Department of Chemical Engineering, Massachusetts Institute of Technology, 77 Massachusetts Avenue, Cambridge, Massachusetts, 02139, USA. E-mail: tahatton@mit.edu; rutledge@mit.edu

† Electronic supplementary information (ESI) available. See DOI: 10.1039/c3ta13361c

integrating conducting polymers[8–13,15] or metal oxides[15,17–22] with other components rely heavily on electrochemical deposition or co-deposition of their precursors (*i.e.*, solubilized monomers or metal ions, respectively). These methods use electrochemical synthesis conditions to manipulate the nanostructures and thus electrocapacitive properties of the resulting heterogeneous materials. As such, these strategies require the use of complicated electrochemical set-ups and sometimes multi-step post-processing such as template removal,[15] and thus can be time-consuming, of low throughput, and difficult to scale up.

Here we show that a metallocene-containing polymer, polyvinylferrocene (PVF), can be integrated with pristine carbon nanotubes (CNTs) *via* a simple, rapid, scalable, solution-based process for the development of hybrid supercapacitors with composition-dependent nanostructures and electrochemical properties. The hybrid with an optimized composition exhibits a unique heterogeneous nanostructure, which consists of a three-dimensional conductive CNT framework with conformal coating of the metallocene polymer. This structure simultaneously facilitates electronic/ionic transport and enhances metallocene utilization efficiency. Therefore this hybrid shows significantly improved energy storage properties compared to those of the individual components alone. The solution processability of the PVF/CNT system is due to its unique ability to form stable, well-dispersed multi-component inks through the noncovalent, π–π stacking interactions between the ferrocene cyclopentadiene (Cp) rings in PVF and the sp^2-conjugated CNT surfaces.[33] Such π–π stacking interactions generally exist between various conductive nanocarbons with sp^2-conjugated surfaces (*e.g.*, graphene, fullerenes, and CNTs) and molecular systems containing metallocenes with Cp rings (*e.g.*, MCp_2, M = Fe, Co, Mn, V, Cr, *etc.*) that can undergo fast and reversible redox reactions. Therefore, in contrast to conducting polymer- and metal oxide-based pseudocapacitive composite materials, the metallocene/carbon system represents a new class of heterogeneous energy-storage materials that is amenable to solution-based construction. In addition, the metallocene/carbon system enjoys several other advantages for the development of high-performance supercapacitors. Firstly, in contrast to chemical modification, the noncovalent assembly method maintains the sp^2-conjugated surfaces of nanocarbons, which is essential for facilitating electron transport in the hybrids. Secondly, the fabrication process is binder-free, surfactant-free, and substrate-independent. Therefore, it avoids issues associated with surfactant removal (such as reducing conductivity and mechanical integrity of the deposited film), and can be extended to stretchable substrates, making it useful for the development of flexible electronics.[29]

Results and discussion

The PVF/CNT hybrids are fabricated through deposition of the PVF/CNT dispersions (obtained *via* gentle sonication) onto solid substrates followed by solvent evaporation (Fig. 1a). For experimental details, see ESI Section S1.2.† The nanoscale architecture of the resulting hybrid can be manipulated systematically by adjusting the PVF/CNT mass ratio in the precursor

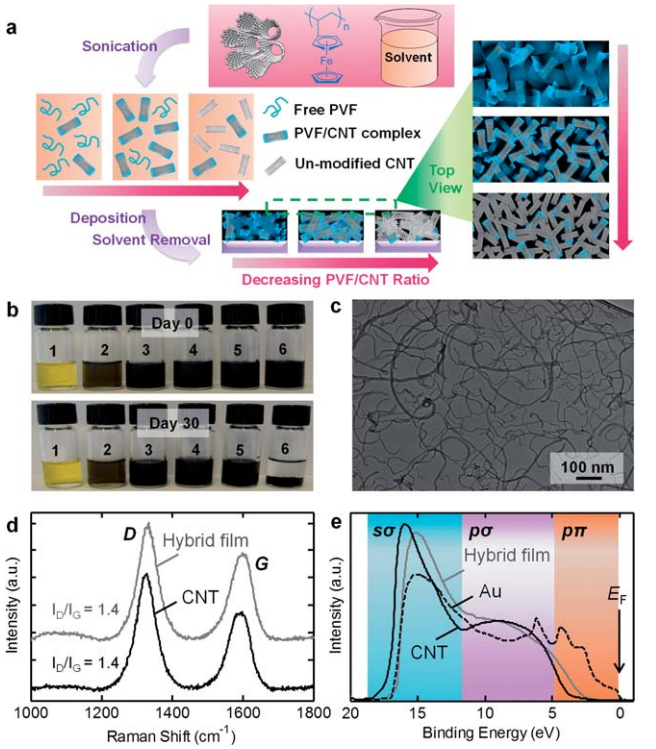

Fig. 1 (a) Schematics of the solution-based process to fabricate PVF/CNT hybrids with different morphologies. (b) Optical photos of PVF/CNT dispersions in chloroform on day 0 and day 30: from vial #1 to #6, CNT at 0, 0.03, 0.20, 0.67, 0.88, 0.20 mg mL^{-1} and PVF at 1, 0.97, 0.80, 0.33, 0.12, 0 mg mL^{-1}. (c) A TEM image of a PVF/CNT dispersion (0.80 mg mL^{-1} PVF and 0.20 mg mL^{-1} CNT). (d) Raman and (e) UPS spectra of a hybrid film (the weight ratio of polymer to CNT is 4 : 1) and pristine CNTs. Gold was used as the internal standard to locate the Fermi level (0 eV) in the UPS measurements.

dispersion before deposition. As this ratio decreases, the dominant species in the dispersion changes from free polymers, to PVF/CNT complexes, to non-functionalized CNTs. This leads to morphological transitions in the deposited hybrids from a thick polymer film with buried nanotubes, to a porous CNT network with conformal polymer coating, to a CNT mat with little polymer exposed. Fig. 1b shows that in the absence of PVF, the suspended CNTs precipitate out within a few days, whereas the PVF/CNT dispersions of various compositions exhibit good stability over at least a month, which is sufficient for the rapid fabrication process. A typical transmission electron microscopy (TEM) image (Fig. 1c) of a PVF/CNT dispersion (0.80 mg mL^{-1} PVF and 0.20 mg mL^{-1} CNT) shows that most CNTs are completely de-bundled individual tubes. PVF/CNT inks with other compositions exhibit similarly good nanotube dispersibility when inspected by TEM. Raman spectra (Fig. 1d) show that the I_D/I_G ratio of the deposited hybrid film remains the same as that of pristine CNTs (for calculation of this ratio, see ESI Section S1.8†). This indicates that our noncovalent assembly method does not generate additional sp^3 defects on CNT surfaces, in contrast to covalent modification of nanotubes that generally leads to an increased I_D/I_G ratio.[34] X-ray diffraction (XRD) results suggest that the nanotube lattice structure is not impaired during fabrication (Fig. S8†). Ultraviolet

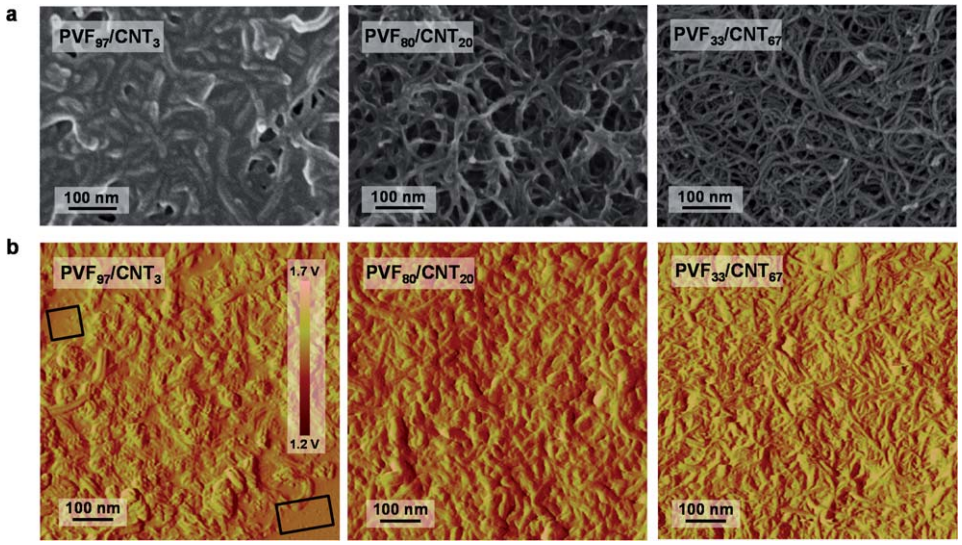

Fig. 2 (a) HR-SEM images and (b) AFM amplitude images of PVF_{97}/CNT_3, PVF_{80}/CNT_{20}, and PVF_{33}/CNT_{67}.

photoelectron spectra (UPS) (Fig. 1e) show that the valence band structure of the hybrid film resembles that of untreated CNTs. Both exhibit a broad peak from 0 to 12 eV and a sharp peak from 12 to 17 eV, corresponding to mixed pπ–pσ bands and s-like σ bands, respectively.[35,36] This indicates that the electronic structure of the nanotube component is mostly preserved during fabrication of the hybrid; by contrast, chemical treatments of CNTs drastically change the nanotube band structure.[37,38] A higher density of π electronic states (0–5 eV)[35,36] in the hybrid, compared to that in pristine CNTs, is possibly due to the surface adsorbed ferrocene that has a strong π electron-donating ability.[39] A larger work function of the hybrid (4.54 ± 0.06 eV) than that of untreated CNTs (3.95 ± 0.02 eV), calculated from their UPS spectra (ESI Section S1.9†), may be attributed to an induced dipole on the nanotube surfaces generated by the negatively-charged Cp rings; this dipole opposes electron emission from CNTs, thereby increasing the work function.[40] This also confirms that the Cp rings of PVF are responsible for its molecular-level interaction with CNTs, consistent with our previous analysis.[33]

The morphologies of the PVF/CNT hybrids with various compositions were investigated by high-resolution scanning electron microscopy (HR-SEM) and atomic force microscopy (AFM). The HR-SEM images (Fig. 2a) reveal a remarkable morphological transition of the hybrids when the polymer weight percent decreases from 97% to 80% to 33%. In PVF_{97}/CNT_3, the CNTs are buried deeply in the polymer films. In contrast, PVF_{80}/CNT_{20} exhibits interconnected nanopores with conformal polymer coating around a three-dimensional nanotube framework. The morphology of PVF_{33}/CNT_{67} is very similar to that of a deposited mat composed only of unmodified CNTs (Fig. S9†), suggesting that the extent of polymer functionalization on nanotubes in this hybrid is very low and that there may be plentiful unmodified nanotubes exposed on the surface. The AFM (amplitude) images (Fig. 2b) show a general trend of decreasing tube diameters with lower PVF content, in accord with the observations from HR-SEM. However, the diameter difference between PVF_{97}/CNT_3 and PVF_{80}/CNT_{20}, as probed by AFM, is not as obvious as the difference revealed by HR-SEM. Notably, the average tube diameters for PVF_{80}/CNT_{20} shown in the AFM image appear slightly larger than the diameters shown in the HR-SEM image. This may be due to artifactual broadening of the AFM scan since the tip cannot penetrate the pores to measure the surface of the CNT framework accurately. For PVF_{97}/CNT_3 and PVF_{33}/CNT_{67}, the average tube diameters are consistent between the HR-SEM and AFM analyses, possibly because these two hybrids exhibit fewer surface features, and thus the tip broadening effects are not pronounced. Moreover, in the AFM image of PVF_{97}/CNT_3, we observe some areas with almost no AFM contrast (as indicated by the black rectangles), which resemble the image of a pure PVF film (Fig. S10†). This suggests existence of pure polymer regions without effective nanotube penetration.

The surface chemical compositions of the PVF/CNT hybrids are probed by X-ray photoelectron spectroscopy (XPS). Fig. 3 shows the Fe/C ratios obtained on the surfaces of the hybrids as a function of CNT weight percent, calculated from their XPS spectra. For XPS quantification details, see ESI Section S1.5.† Pure PVF has a Fe/C ratio of 0.02, while the pristine CNTs have no iron signal (Fe/C ratio = 0). The PVF/CNT hybrids with CNT

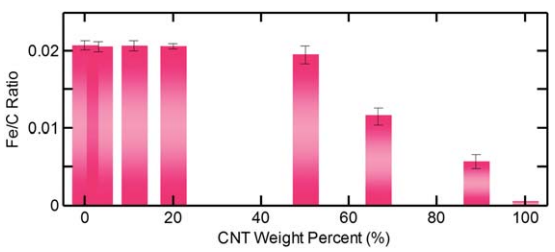

Fig. 3 The Fe/C ratios of the PVF/CNT hybrids with varying compositions, calculated from their XPS spectra. Error bar: s.d. from three or four samples.

content ranging from 3% to 50% have the same Fe/C ratios as the pure polymer. This indicates that the surfaces of these hybrids are covered completely by PVF. It is of particular importance that PVF_{80}/CNT_{20} has the same surface chemical composition as the neat polymer, despite its highly porous nanostructure, revealed by HR-SEM. This indicates that the CNT scaffold is coated *conformally* by PVF, and almost no unmodified nanotubes are exposed on the surface. In contrast, when the CNT weight percentages are as high as 67% and 90%, the Fe/C ratios decrease markedly to 0.012 and 0.005, respectively. This suggests that the surfaces of these two hybrid systems are only covered partially by the redox polymer and consist of both PVF-coated and non-functionalized CNTs.

We performed electrochemical characterization of the hybrids, deposited on conductive carbon substrates, in a three-electrode system with 0.5 M $NaClO_4$ as the electrolyte. Fig. 4a shows the specific capacitances of the PVF/CNT hybrids as a function of CNT weight percent. PVF alone shows a low capacitance value of 57 F g^{-1}. This is probably due to its low conductivity and small surface area, and suggests inefficient utilization of the redox-active ferrocene moieties. The pristine CNTs also have a very low specific capacitance of 16 F g^{-1}. Remarkably, the PVF/CNT hybrids exhibit significantly greater capacitances than either component alone, with a peak value of 335 F g^{-1} at a nanotube composition of 20 wt%. This optimal capacitance value may be attributed to the unique morphology of PVF_{80}/CNT_{20} (Fig. 2), in which the three-dimensional porous CNT network is coated conformally with PVF. The highly conductive CNT framework facilitates electron transport to favor the redox transformation of ferrocene, while the porous structure allows easy ion diffusion into the polymer layer. Moreover, the conformality of the polymer coating exposes a high density of redox sites to the electrolyte solution, thus improving the efficacy of metallocene usage. When the CNT weight percent is further increased to 67%, the polymer coating is less obvious (Fig. 2, PVF_{33}/CNT_{67}), indicating a low concentration of ferrocene moieties exposed on the surface. The content of the energy-dense polymer for this hybrid is much lower than that of PVF_{80}/CNT_{20}, thereby giving rise to a reduced capacitance of 109 F g^{-1}. On the other hand, when the nanotube content is as low as 3%, the ferrocene sites may not be completely used for energy storage because the thick polymer films are not effectively penetrated by CNTs, and display limited porosity (Fig. 2, PVF_{97}/CNT_3). Therefore, in this case, even though the polymer content is higher than that of PVF_{80}/CNT_{20}, the capacitance is reduced to a lower value of 179 F g^{-1}.

The dramatically improved energy storage capacity of the hybrids can be appreciated directly by comparing their cyclic voltammograms (CVs) and galvanostatic profiles with those of pure PVF and pristine CNTs, respectively. The CV curves are illustrated in Fig. 4b. CNTs alone exhibit a rectangular voltammogram, characteristic of double-layer capacitive materials. The CVs of PVF-containing electrodes have two pronounced peaks, corresponding to the redox reactions of the ferrocene molecules. Compared to pure PVF and CNTs, the three hybrids exhibit significantly enhanced current response; among them, PVF_{80}/CNT_{20} exhibits the highest current density. The galvanostatic measurements are shown in Fig. 4c. The neat CNT sample exhibits a linear decrease with time over the entire potential range from 0.8 to 0.0 V, whereas ferrocene-containing samples display sloped plateaus between 0.4 and 0.2 V, corroborating their pseudocapacitive charge storage behavior. PVF_{80}/CNT_{20} shows the longest discharge time, indicating that it has the highest capacitance among all samples. Additionally, CV measurements with varying scan rates (Fig. S11†) and galvanostatic experiments with different current densities (Fig. S12†) confirm that incorporation of CNTs into PVF improves the capacitance value in the order: PVF < PVF_{33}/CNT_{67} < PVF_{97}/CNT_3 < PVF_{80}/CNT_{20}, under all the operational conditions tested.

Based on the initial screening, we found that PVF_{80}/CNT_{20} exhibits remarkable synergistic effects with significantly better energy storage capabilities relative to those of the two individual components. Energy-dense pseudocapacitive systems generally exhibit much higher capacitance values than double-layer capacitive materials.[1,2,5] Therefore it is easy to understand that, relative to CNTs, this hybrid shows better capacitive performance since its composition contains a large fraction of the redox-active metallocene polymer. When comparing the hybrid to neat PVF, the question of how effectively the ferrocene moieties are used for electrochemical energy storage becomes important, since inactive ferrocene molecules that cannot undergo redox reactions have no pseudocapacitance contribution. Chronocoulometry was used to quantify the ferrocene

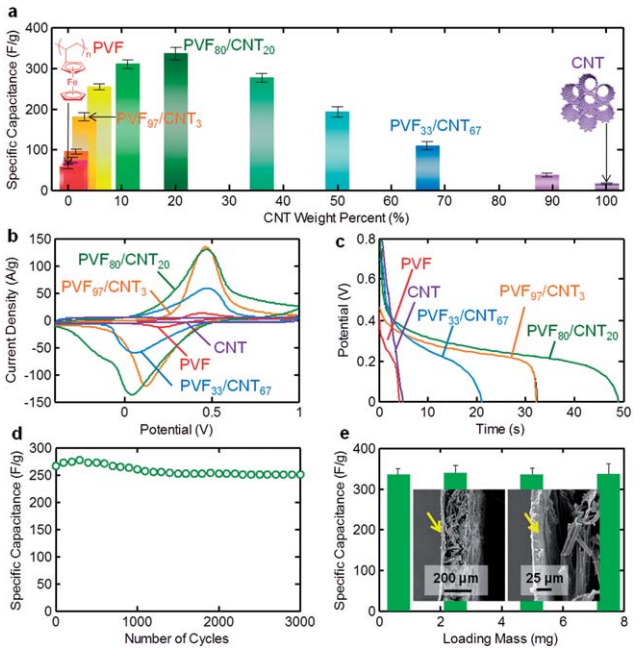

Fig. 4 (a) The specific capacitance as a function of CNT composition, in weight percent. The capacitances were calculated from CVs at 20 mV s^{-1}. Error bar: s.d. from three samples. (b) CVs at 200 mV s^{-1} and (c) galvanostatic discharge profiles at 5 A g^{-1} for pure CNTs, neat PVF, PVF_{33}/CNT_{67}, PVF_{97}/CNT_3, and PVF_{80}/CNT_{20}. (d) Capacitance *versus* the number of charge/discharge cycles for PVF_{80}/CNT_{20}. (e) Specific capacitance of PVF_{80}/CNT_{20} as a function of loading mass. Insets show the cross-sectional SEM images of the deposited film at a loading mass of 750 μg with two different magnifications. The arrows indicate the PVF_{80}/CNT_{20} layer.

utilization efficiency (FUE) for PVF and PVF_{80}/CNT_{20}, defined as the ratio of the observed charge due to ferrocene oxidization to the theoretical value when all ferrocene molecules are oxidized (for details, see ESI Section S1.6†). We found that the FUE for PVF_{80}/CNT_{20} (63%) is improved markedly compared to that for PVF alone (8%). This improvement is believed to be attributable to conformality of the polymer coating around the CNT scaffold. This places more ferrocene in contact with both the electrolyte solution and the conductive framework, and thus more ferrocene molecules are electrochemically active.[41] Assuming that the CNT component has a nearly negligible capacitance contribution in the hybrid (note that the neat CNT sample has a very low capacitance value of 16 F g^{-1}), the ratio of FUE times polymer wt% between PVF_{80}/CNT_{20} and PVF (63% × 80%/(8% × 100%) = 6.3) explains well the capacitance amplification factor between them (335 F g^{-1}/57 F g^{-1} = 5.9). Another intriguing advantage of the hybrid over the neat PVF film is its highly porous structure; this may reduce ion-transport resistance, which is the key to enhancing rate performance for high-power applications. The Brunauer–Emmett–Teller (BET) surface area of PVF_{80}/CNT_{20} (112 m^2 g^{-1}) is found to be much higher than that of the pure PVF film (8 m^2 g^{-1}), consistent with the greatly increased porosity of the hybrid observed by HR-SEM. Electrochemical impedance spectroscopy (EIS) measurements confirm that the charging resistance in the hybrid is significantly lower than that in PVF (ESI Section S1.7†). This may be attributed to the interconnected nanopores with sizes ~100 nm observed in the PVF_{80}/CNT_{20} hybrid (Fig. 2) that reduce the characteristic length scale for ion diffusion and thus result in efficient charge propagation.

The cycling stability of PVF_{80}/CNT_{20} was investigated by constant current charge/discharge experiments at a current density of 5 A g^{-1}. Fig. 4d shows that its specific capacitance decreased by only 8% after 1500 cycles, and remained constant thereafter, up to 3000 cycles, demonstrating very good electrochemical stability. In contrast, the capacitance of PVF decayed by 62% after 1500 cycles. The improved cycling stability of PVF_{80}/CNT_{20} may be attributed to the mechanical integrity of the interconnected nanotubes, which support the polymer layers and prevent large morphological changes during the charge/discharge process.

It has been observed previously that the specific capacitance of supercapacitors decreases when the loading mass and the thickness of the active material increase, possibly due to the increased electrolyte transport limitation associated with thicker films.[29] Therefore the capacitive performance of a supercapacitor should be evaluated when the thickness of the active materials is equal to or larger than the suggested value for commercial supercapacitor devices. Fig. 4e shows that the specific capacitance of PVF_{80}/CNT_{20} remains almost unchanged when its loading mass increases progressively from 62.5 to 750 μg, at which point the thickness of the deposited film reaches a value of ~22 μm (Fig. 4e inset). This is already larger than the recommended thickness of 15 μm for commercial supercapacitors.[42] This may be attributed to the highly porous nanostructure of the hybrid and low ion transport resistance, as discussed earlier. In addition, we found that the effects of the substrate on the electrochemical performance of the PVF/CNT hybrid are negligible (Fig. S13†).

Finally, we constructed a supercapacitor cell with a hybrid of the optimized composition (*i.e.*, PVF_{80}/CNT_{20}) using a symmetrical two-electrode configuration (for details, see ESI Section S1.4†). For comparison, a supercapacitor cell with neat PVF was also constructed. CV measurements in 0.5 M $NaClO_4$ (Fig. 5a, black data) show that both PVF_{80}/CNT_{20} and PVF exhibit non-rectangular voltammograms, indicative of pseudocapacitive behavior. A significantly higher current with PVF_{80}/CNT_{20} compared to that with PVF confirms the prominent advantage of using heterogeneous nanostructures. The corresponding capacitance as a function of scan rate is shown in Fig. 5b (black data). These values are different from those obtained in a three-electrode configuration (Fig. 4a), as is typical for pseudocapacitive materials; it has been suggested that the true performance of electrocapacitive systems should be assessed in a two-electrode configuration.[42,43] Detailed comparison between the two types of electrode configurations is discussed by Stoller and Ruoff.[42]

It is well-known that the type of electrolyte has a significant effect on supercapacitor performance. Acidic electrolytes generally result in remarkably higher capacitance than do neutral electrolytes.[44,45] A large body of literature reports the capacitance value obtained in H_2SO_4 (Table S2†). The reason for this is not completely clear; however, it has been suggested that proton hopping *via* the hydrogen-bonding networks of water molecules (*i.e.*, the Grotthuss mechanism) on the surfaces of capacitive materials can improve charge storage capacity.[45–47] This motivated a test of cell performance using H_2SO_4 as the electrolyte. The resulting CV curves and capacitance values are shown in Fig. 5a and b (green data), respectively. The CV current densities and capacitances are remarkably higher than those obtained in $NaClO_4$. The performance disparity in different electrolytes can be attributed partially to the aforementioned proton hopping mechanism. Another contributing factor may

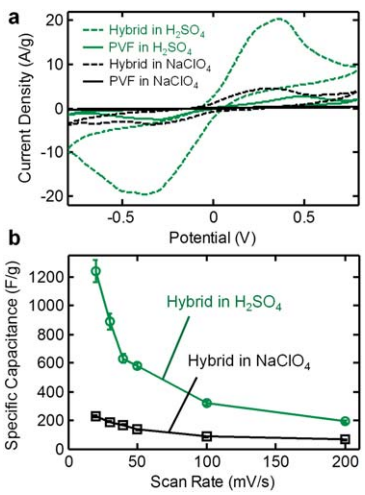

Fig. 5 (a) CVs at 20 mV s^{-1} of PVF_{80}/CNT_{20} and PVF obtained in a symmetrical two-electrode supercapacitor cell in different electrolyte solutions. (b) The specific capacitance of PVF_{80}/CNT_{20} at different scan rates.

be related to the nature of the anion and its interaction with the PVF polymer. Compared to SO_4^{2-}, ClO_4^- can ion pair more strongly with ferrocenium cations,[48,49] which leads to collapsed polyelectrolytes due to strong screening effects and counterion condensation.[50] This collapse hinders electron transport and ion diffusion, resulting in significantly reduced electrode currents.[51] The stronger propensity of ClO_4^- to ion pair with ferrocenium than that of SO_4^{2-} is not due to their ion sizes (both having anionic thermochemical radii ~0.24 nm), but should be attributed to their dramatically different energies of hydration (−205 kJ mol^{-1} for ClO_4^- and −1295 kJ mol^{-1} for SO_4^{2-}).[52] The more hydrophobic ClO_4^- has a stronger tendency to strip off the surrounding water molecules to bind with the ferrocenium cations than does the relatively hydrophilic SO_4^{2-}. In fact, the effective formation constants for ion pairs between ferrocenium and different anions have been shown to scale approximately with the solvation energies of the anions.[48] This relationship suggests that an anion with a less negative solvation energy binds to ferrocenium more easily. The maximum capacitance obtained using the PVF_{80}/CNT_{20} supercapacitor cell with 1 M H_2SO_4 (1241 F g^{-1} at 20 mV s^{-1}) is comparable to the highest values reported to date measured in a two-electrode configuration (*e.g.*, 911 F g^{-1} for brush-like Co_3O_4,[53] and 1145 F g^{-1} for MnO_2/nanoporous gold).[20] It should be noted that several previously reported high capacitance values (>1000 F g^{-1}) based on conducting polymers[10–12] and metal oxides[16,19,21,22] are obtained in a three-electrode configuration, which can be subject to errors in the measurement of capacitance, in particular for pseudocapacitive systems.[42] See Table S2† for a complete list of the electrocapacitve performance of different pseudocapacitive materials.

To further evaluate the energy and power densities of PVF_{80}/CNT_{20}, we carried out galvanostatic measurements in 1 M H_2SO_4, which have been considered the most accurate method for determining the performance of supercapacitor materials.[42] The hybrid exhibits non-linear pseudocapacitive discharge profiles at different current densities (Fig. 6a). The specific capacitances calculated from the galvanostatic experiments are shown in Fig. 6b. The capacitance values agree well with those derived from CV measurements (Fig. 5b). Moreover, it can be seen from Table S2† that most previously reported high capacitance values were obtained at low operation rates (less than 1 A g^{-1}). Therefore, PVF_{80}/CNT_{20} exhibits the best combination of a high capacitance and a high operation rate (1450 F g^{-1} at 20 A g^{-1}) among currently available pseudocapacitive materials. We attribute this to its unique nanosized hybrid architecture that allows easy and efficient transport of both electrons and ions, which in turn affords fast redox reactions at high rates. Fig. 6c shows the Ragone plot for PVF_{80}/CNT_{20} and the power and energy density ranges for common classes of energy storage devices.[54] The energy density was estimated either from $1/2CV^2$ (black squares) or from $i \times \int v(t)dt$ (gray circles) (for details, see ESI Section 1.4†). It can be clearly seen from Fig. 6c that the energy densities of the PVF_{80}/CNT_{20}-based device are comparable to those of batteries, while its power densities are maintained at values as high as those observed with conventional electrolytic capacitors.[54] The maximum energy density (79.5 W h kg^{-1}, obtained using the more conservative integration method) represents the highest reported value among pseudocapacitive materials in aqueous electrolytes with a typical electrochemical window ~1 V (Table S2†).

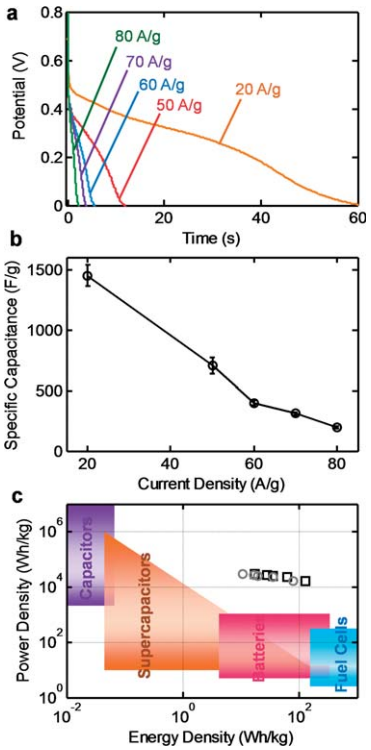

Fig. 6 (a) Galvanostatic discharge profiles of PVF_{80}/CNT_{20} at different current densities obtained in a symmetrical two-electrode supercapacitor cell in 1 M H_2SO_4. (b) Specific capacitance *versus* current density, derived from galvanostatic measurements. Error bar: s.d. of three samples. (c) Ragone plot (power density *versus* energy density). The data for PVF_{80}/CNT_{20} are shown either in black or in gray, depending on the calculation method. The ranges reported for common classes of energy storage devices[45] are also depicted.

Conclusion

We have developed a metallocene/carbon hybrid system that can be constructed by an economical, rapid, scalable, solution-based process for supercapacitor applications. The nanostructure and electrochemical properties of this hybrid can be manipulated systematically by adjusting the composition of the precursor dispersion before deposition. The ease of assembly of the metallocene/carbon hybrid contrasts sharply with that of metal oxide- and conducting polymer-based heterogeneous systems, in which their controlled assembly relies heavily on electrochemical deposition processes that are low-throughput and hard to scale up. Moreover, the PVF/CNT hybrid with the optimized composition exhibits a highly porous nanoscale architecture in which a three-dimensional conductive carbon nanotube network with interconnected nanopores is coated conformally by the redox-active metallocene polymer. This unique morphology simultaneously facilitates electron transport, reduces ion diffusion length, and increases metallocene utilization efficiency. Thus this hybrid exhibits significantly

improved electrochemical performance compared to those of the neat individual components. A standard two-electrode supercapacitor cell constructed with this hybrid system shows extremely high specific capacitance and energy density. The exceptional electrocapacitive energy storage capabilities of the metallocene/carbon hybrid, accompanied by its unique solution processability, make it an excellent material system for the development of low-cost high-performance supercapacitors.

Acknowledgements

This work is supported by the U.S. Department of Energy and an MITEI Seed Fund Grant. The authors thank Xiao Su for technical assistance with the XPS measurements, and Yuran Wang for the XRD measurements.

Notes and references

1 P. Simon and Y. Gogotsi, *Nat. Mater.*, 2008, **7**, 845.
2 G. P. Wang, L. Zhang and J. J. Zhang, *Chem. Soc. Rev.*, 2012, **41**, 797.
3 J. R. Miller and P. Simon, *Science*, 2008, **321**, 651.
4 Y. P. Zhai, Y. Q. Dou, D. Y. Zhao, P. F. Fulvio, R. T. Mayes and S. Dai, *Adv. Mater.*, 2011, **23**, 4828.
5 X. Zhao, B. M. Sanchez, P. J. Dobson and P. S. Grant, *Nanoscale*, 2011, **3**, 839.
6 R. Liu, J. Duay and S. B. Lee, *Chem. Commun.*, 2011, **47**, 1384.
7 A. L. M. Reddy, S. R. Gowda, M. M. Shaijumon and P. M. Ajayan, *Adv. Mater.*, 2012, **24**, 5045.
8 Z. Q. Niu, P. S. Luan, Q. Shao, H. B. Dong, J. Z. Li, J. Chen, D. Zhao, L. Cai, W. Y. Zhou, X. D. Chen and S. S. Xie, *Energy Environ. Sci.*, 2012, **5**, 8726.
9 M. Ertas, R. M. Walczak, R. K. Das, A. G. Rinzler and J. R. Reynolds, *Chem. Mater.*, 2012, **24**, 433.
10 H. Zhang, G. Cao, Z. Wang, Y. Yang, Z. Shi and Z. Gu, *Electrochem. Commun.*, 2008, **10**, 1056.
11 M. A. Q. Xue, F. W. Li, J. Zhu, H. Song, M. N. Zhang and T. B. Cao, *Adv. Funct. Mater.*, 2012, **22**, 1284.
12 L. Z. Fan, Y. S. Hu, J. Maier, P. Adelhelm, B. Smarsly and M. Antonietti, *Adv. Funct. Mater.*, 2007, **17**, 3083.
13 D.-W. Wang, F. Li, J. Zhao, W. Ren, Z.-G. Chen, J. Tan, Z.-S. Wu, I. Gentle, G. Q. Lu and H.-M. Cheng, *ACS Nano*, 2009, **3**, 1745.
14 Y. G. Wang, H. Q. Li and Y. Y. Xia, *Adv. Mater.*, 2006, **18**, 2619.
15 R. Liu and S. B. Lee, *J. Am. Chem. Soc.*, 2008, **130**, 2942.
16 Z. Tang, C. H. Tang and H. Gong, *Adv. Funct. Mater.*, 2012, **22**, 1272.
17 H. Zhang, G. P. Cao, Z. Y. Wang, Y. S. Yang, Z. J. Shi and Z. N. Gu, *Nano Lett.*, 2008, **8**, 2664.
18 L. B. Hu, W. Chen, X. Xie, N. A. Liu, Y. Yang, H. Wu, Y. Yao, M. Pasta, H. N. Alshareef and Y. Cui, *ACS Nano*, 2011, **5**, 8904.
19 X. Wang, A. Sumboja, M. F. Lin, J. Yan and P. S. Lee, *Nanoscale*, 2012, **4**, 7266.
20 X. Y. Lang, A. Hirata, T. Fujita and M. W. Chen, *Nat. Nanotechnol.*, 2011, **6**, 232.
21 C. Z. Yuan, L. Yang, L. R. Hou, L. F. Shen, X. G. Zhang and X. W. Lou, *Energy Environ. Sci.*, 2012, **5**, 7883.
22 Q. Li, Z. L. Wang, G. R. Li, R. Guo, L. X. Ding and Y. X. Tong, *Nano Lett.*, 2012, **12**, 3803.
23 J. Y. Kim, K. Lee, N. E. Coates, D. Moses, T. Q. Nguyen, M. Dante and A. J. Heeger, *Science*, 2007, **317**, 222.
24 U. Bach, D. Lupo, P. Comte, J. E. Moser, F. Weissortel, J. Salbeck, H. Spreitzer and M. Gratzel, *Nature*, 1998, **395**, 583.
25 J. H. Ahn, H. S. Kim, K. J. Lee, S. Jeon, S. J. Kang, Y. G. Sun, R. G. Nuzzo and J. A. Rogers, *Science*, 2006, **314**, 1754.
26 D. V. Talapin and C. B. Murray, *Science*, 2005, **310**, 86.
27 X. F. Duan, C. M. Niu, V. Sahi, J. Chen, J. W. Parce, S. Empedocles and J. L. Goldman, *Nature*, 2003, **425**, 274.
28 P. Poizot, S. Laruelle, S. Grugeon, L. Dupont and J. M. Tarascon, *Nature*, 2000, **407**, 496.
29 L. B. Hu, J. W. Choi, Y. Yang, S. Jeong, F. La Mantia, L. F. Cui and Y. Cui, *Proc. Natl. Acad. Sci. U. S. A.*, 2009, **106**, 21490.
30 K. H. An, W. S. Kim, Y. S. Park, Y. C. Choi, S. M. Lee, D. C. Chung, D. J. Bae, S. C. Lim and Y. H. Lee, *Adv. Mater.*, 2001, **13**, 497.
31 X. F. Lu, W. J. Zhang, C. Wang, T. C. Wen and Y. Wei, *Prog. Polym. Sci.*, 2011, **36**, 671.
32 C. D. Lokhande, D. P. Dubal and O. S. Joo, *Curr. Appl. Phys.*, 2011, **11**, 255.
33 X. Mao, G. C. Rutledge and T. A. Hatton, *Langmuir*, 2013, **29**, 9626.
34 N. Lachman, X. M. Sui, T. Bendikov, H. Cohen and H. D. Wagner, *Carbon*, 2012, **50**, 1734.
35 N. P. Blanchard, R. A. Hatton and S. R. P. Silva, *Chem. Phys. Lett.*, 2007, **434**, 92.
36 S. Suzuki, Y. Watanabe, T. Kiyokura, K. G. Nath, T. Ogino, S. Heun, W. Zhu, C. Bower and O. Zhou, *Phys. Rev. B: Condens. Matter Mater. Phys.*, 2001, **63**, 245418.
37 J. J. Zhao, H. K. Park, J. Han and J. P. Lu, *J. Phys. Chem. B*, 2004, **108**, 4227.
38 C. C. Wang, G. Zhou, J. Wu, B. L. Gu and W. H. Duan, *Appl. Phys. Lett.*, 2006, **89**, 173130.
39 T. Wakahara, M. Sathish, K. Miyazawa, C. P. Hu, Y. Tateyama, Y. Nemoto, T. Sasaki and O. Ito, *J. Am. Chem. Soc.*, 2009, **131**, 9940.
40 T. C. Leung, C. L. Kao, W. S. Su, Y. J. Feng and C. T. Chan, *Phys. Rev. B: Condens. Matter Mater. Phys.*, 2003, **68**, 195408.
41 T. Chen, L. Wang, G. H. Jiang, J. J. Wang, X. C. Dong, X. J. Wang, J. F. Zhou, C. L. Wang and W. Wang, *J. Phys. Chem. B*, 2005, **109**, 4624.
42 M. D. Stoller and R. S. Ruoff, *Energy Environ. Sci.*, 2010, **3**, 1294.
43 K. V. E. Frackowiak and F. Beguin, *Electrochim. Acta*, 2005, **50**, 2499.
44 G. Lota, K. Fic and E. Frackowiak, *Energy Environ. Sci.*, 2011, **4**, 1592.
45 C. C. Hu and C. C. Wang, *J. Power Sources*, 2004, **125**, 299.
46 N. Agmon, *Chem. Phys. Lett.*, 1995, **244**, 456.
47 W. Gao, N. Singh, L. Song, Z. Liu, A. L. M. Reddy, L. J. Ci, R. Vajtai, Q. Zhang, B. Q. Wei and P. M. Ajayan, *Nat. Nanotechnol.*, 2011, **6**, 496.

48 G. K. Rowe and S. E. Creager, *Langmuir*, 1991, **7**, 2307.
49 P. K. Eggers, P. Da Silva, N. A. Darwish, Y. Zhang, Y. J. Tong, S. Ye, M. N. Paddon-Row and J. J. Gooding, *Langmuir*, 2010, **26**, 15665.
50 R. G. Winkler, M. Gold and P. Reineker, *Phys. Rev. Lett.*, 1998, **80**, 3731.
51 E. Y. Choi, O. Azzaroni, N. Cheng, F. Zhou, T. Kelby and W. T. S. Huck, *Langmuir*, 2007, **23**, 10389.
52 B. A. Moyer and P. V. Bonnesen, Physical Factors in Anion Separation, in *Supramolecular Chemistry of Anions*, ed. A. Bianchi, K. Bowman-James and E. Garcia-Espana, Wiley-VCH, Inc., New York, 1979, pp. 1–44.
53 R. B. Rakhi, W. Chen, D. Y. Cha and H. N. Alshareef, *Nano Lett.*, 2012, **12**, 2559.
54 A. G. Pandolfo and A. F. Hollenkamp, *J. Power Sources*, 2006, **157**, 11.